# Influence of chromatic dispersion on a dual-wavelength passive-homodyne detection method for fiber-coupled interferometers

Hugues R. Giovannini, Serge J. Huard, and Michel R. Lequime

The passive-homodyne method is very attractive for demodulating optical signals available at the output of interferometric sensors by the use of coherence multiplexing. Phase measurement and the use of two broadband sources with different central wavelengths permit a resolution of $\lambda/10^5$ to be achieved with a 20-μm range-sensor optical path difference. However, dispersive birefringent elements are required in this technique, which has some disturbing effects on the correlation signal position, on its envelope form, and on the measured phase. An analytical treatment of the problem and a numerical validation are described. Experimental evidence of the effects predicted by theory is presented.

*Key words:* Fiber-optic sensor, coherence multiplexing, passive homodyne, birefringence, chromatic dispersion.

## 1. Introduction

Optical fiber sensors are useful in many industrial applications in perturbed environments. In this context the use of interferometric sensors based on the so-called coherence multiplexing technique[1] is a suitable solution to the problem of the sensitivity to source drifts or line-loss variations.[2–4] With this kind of technique a broadband light source is connected by an optical fiber to an interferometric sensor for which the optical path difference (OPD) is much greater than the source coherence length and is related to the parameter to be measured. After going through a demodulation interferometer whose OPD is close to the sensor OPD, the output light flux is sent to a receiver (photodetector). Thus detection in the Fourier space is used to recover the parameter.[5] The signal provided by the receiver appears to be the sum of a dc component and a sine term whose phase is related to the parameter. The demodulation system described in this paper consists of two parallel interferometers in quadrature, each with two complementary outputs. The four signals (two per channel) are then processed to calculate the phase of the sine function. This configuration makes up the passive-homodyne[6] demodulator, and a two-wavelength measurement is used to increase the range.[7] With this kind of method the interferometer used to demodulate the sensing interferometer must be as stable as possible; therefore the two interferometers may have different optical characteristics. Because of the use of broadband light sources, which are typically light-emitting diodes (LED's), effects on the measurement from the spectral dependence of the optical properties of the sensor and the demodulator are not negligible. We analyze in this paper both the influence of the chromatic dependence of the OPD in the interferometers and the influence of the chromatic dispersion of the quarter-wave retarder used in one channel of the demodulator. In both cases we take an analytical approach in describing the effects. A numerical simulation is also used to predict the results obtained experimentally.

## 2. Operating Principle

In a measurement device that uses coherence multiplexing, a LED is connected by optical fiber to an interferometric sensor for which the OPD $\Delta_s$ is much greater than the source coherence length; $\Delta_s$ is supposed to be related to the parameter $X$ to be measured. The output light flux goes through a demodulation

H. R. Giovanni and S. J. Huard are with the Laboratoire des Surfaces et Couches Minces, Unité de Récherche Associée 1120 Centre National de la Recherche Scientifique, Ecole Normale Supérieure de Physique de Marseille, Domaine Universitaire de Saint-Jerome, 13397 Marseille Cedex 20, France; M. R. Lequime is with the Société Bertin et Cie, 230, rue Frédéric Joliot, Z. I. Les Milles, B. P. 22000, 13791 Aix-en-Provence, France.

Received 4 August 1992; revised manuscript received 20 September 1993.

0003-6935/94/132721-13$06.00/0.

interferometer whose OPD $\Delta_d$ is close to $\Delta_s$. The signal $S(X)$ provided by the photodetector is then described by

$$S(X) = k_s k_d \int_\sigma P_t(\sigma)T(\sigma)[1 + u_s(\Delta_s)\cos(2\pi\sigma\Delta_s)] \times [1 + u_d(\Delta_d)\cos(2\pi\sigma\Delta_d]\mathrm{d}\sigma, \quad (2.1)$$

where $\sigma$ is the wave number, $k_s$ is a numerical parameter equal to one half for a Michelson-type sensor and one fourth for a birefringent type (unpolarized incident light), $k_d$ is the same parameter as $k_s$ for the demodulation interferometer, $P_t(\sigma)$ is the spectral distribution of the transmitted light, $T(\sigma)$ is the spectral transmission of the whole system, $u_s(\Delta_s)$ is the visibility of the interferometric sensor, $u_d(\Delta_d)$ is the visibility of the demodulation interferometer.

$\Delta_d$ is supposed to be constant, so, noting that

$$P(\sigma) = k_s k_d P_t(\sigma)T(\sigma),$$
$$U = u_s(\Delta_s)u_d,$$

we have

$$S(X) = \int_\sigma P(\sigma)\mathrm{d}\sigma + \frac{1}{2}U\int_\sigma P(\sigma)\cos[2\pi\sigma(\Delta_s - \Delta_d)]\mathrm{d}\sigma. \quad (2.2)$$

When the source is a LED, we can consider $P(\sigma)$ a symmetric function centered on $\sigma_0$. Noting $\phi$, the phase to be measured, by

$$\phi = 2\pi\sigma_0[\Delta_s(X) - \Delta_d], \quad (2.3)$$

$I$, the dc component that corresponds to the continuous background, by

$$I = \tilde{P}(0), \quad (2.4)$$

and $m(\phi)$, the modulation amplitude, by

$$m(\phi) = \frac{1}{2}\frac{U}{I}\tilde{P}(\Delta_s - \Delta_d), \quad (2.5)$$

where $\tilde{P}(x)$ is the cosine transform of the incident light spectral distribution, i.e.,

$$\tilde{P}(x) = \int_\sigma P(\sigma)\cos(2\pi\sigma x)\mathrm{d}\sigma,$$

we have

$$S(X) = I[1 + m(\phi)\cos\phi]. \quad (2.6)$$

The use of a quarter-wavelength plate in the other channel of the demodulator leads to another signal:

$$S'(X) = I[1 + m(\phi)\sin\phi]. \quad (2.7)$$

Thus extraction of $\phi$ from Eqs. (2.6) and (2.7) together with complete knowledge of $\Delta_d$ permits the determination of $\Delta_s$ and then $X$.

### 3. Demodulator Description

The passive-homodyne demodulation principle requires a stable and reliable detection module. Therefore the demodulator (Fig. 1) is chosen to provide four signals: two complementary outputs of the polarimetric interferometer:

$$S_0(X) = I_0[1 + m_0(\phi)\cos\phi],$$
$$S_1(X) = I_1[1 - m_1(\phi)\cos\phi], \quad (3.1a)$$

and two additional outputs in quadrature with the former expressions (owing to a $\pi/2$ retarder),

$$S_2(X) = I_2[1 + m_2(\phi)\sin\phi],$$
$$S_3(X) = I_3[1 - m_3(\phi)\sin\phi]. \quad (3.1b)$$

Note that in this paper we call the demodulator plate the birefringent plate, which permits us to match the OPD of the sensing interferometer in the demodulator.

To recover the phase it is necessary to eliminate the dc components $I_i(i = 1, \ldots, 4)$ and the modulation amplitude terms $m_i(i = 1, \ldots, 4)$; therefore the demodulator system must be calibrated, and the following two stages are carried out. The four signals are analog to digital (A/D) converted and recorded on a computer. At first the light is switched to bypass the sensor, in which case $S_i = I_i(i = 1, \ldots, 4)$ and the ratios $\alpha_1 = I_0/I_1$, $\alpha_1 = I_0/I_2$, and $\alpha_1 = I_0/I_3$ can be computed. Then the light is launched through a calibration interferometer (typically a Michelson interferometer), and the terms

$$S_s(X) = \alpha_2 S_2 - \alpha_3 S_3 = I_0[m_2(\phi) + m_3(\phi)]\sin\phi,$$
$$S_c(X) = S_0 - \alpha_1 S_1 = I_0[m_0(\phi) + m_1(\phi)]\cos\phi\}, \quad (3.2)$$

are computed.

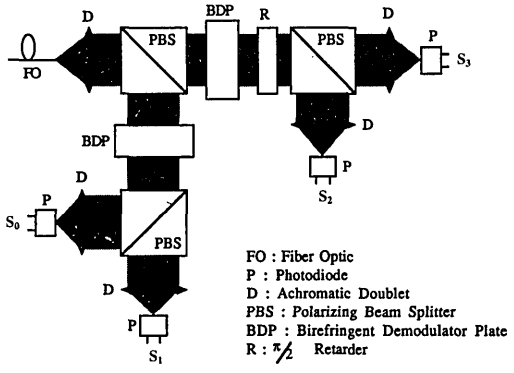


Fig. 1. Demodulator scheme.

The Michelson OPD is changed to record the correlation peak so that we obtain the modulation amplitudes of $S_s$ and $S_c$. Then the ratio

$$\beta = \frac{I_0[m_0(\phi) + m_1(\phi)]}{I_0[m_2(\phi) + m_3(\phi)]} \tag{3.3}$$

is formed; $\beta$ does not depend on $u_s$ and $\phi$, and the calibration is independent of the sensor used. When the demodulator is connected to the sensor the measured phase $\phi_M$ is

$$\phi_M = \tan^{-1}\left(\beta \frac{\alpha_2 S_2 - \alpha_3 S_3}{S_0 - \alpha_1 S_1}\right). \tag{3.4}$$

Note:

(1) The calibration of the dc components, which one can perform between two measurements by using an optical switch, permits one to eliminate the effects from the variations of the detector's sensitivity. Such variations may be caused by thermal fluctuations.

(2) The visibility of each of the four channels of the demodulator is supposed to be constant, and $\beta$ is calibrated only at the factory.

(3) The term $\phi_M$ is independent of the visibility fluctuations of the sensing interferometer and of the source power variations. Moreover the use of a birefringent interferometer in the demodulator saves critical adjustments.

Studying the sign of $\sin\phi$ permits removal of the $\pi$ ambiguity in the value of $\phi_M$ given in Eq. (3.4).

In this case we have

$$\phi_M = 2\pi\sigma_0\Delta(X) \tag{3.5}$$

with

$$\Delta(X) = \Delta_s(X) - \Delta_d. \tag{3.6}$$

By using a dual-wavelength source arrangement, we can measure two phases, $\phi_{M1}$ and $\phi_{M2}$, with

$$\phi_{M1} = \frac{2\pi}{\lambda_1}(\Delta_s - \Delta_d) - 2p_1\pi,$$

$$\phi_{M2} = \frac{2\pi}{\lambda_2}(\Delta_s - \Delta_d) - 2p_2\pi, \tag{3.7}$$

where $p_1$ and $p_2$ are two integers. The differential phase $\Delta\phi = \phi_{M1} - \phi_{M2}$ measurement at the synthetic wavelength

$$\Lambda \frac{\lambda_1\lambda_2}{\lambda_2 - \lambda_1} \tag{3.8}$$

permits us to obtain $p_1$ and to solve the problem of the limited dynamic range caused by the $2\pi$ ambiguity of the single-wavelength phase measurement.[8–10]

#### 4. Influence of Chromatic Dependence on the OPD

So far $\Delta_s$ and $\Delta_d$ have been considered independent of wave number $\sigma$. So far as $\Delta_s$ and $\Delta_d$ have been considered independent of the wave number $\sigma$, which is true for $\Delta_s$ in the case of Michelson-type interferometric sensors; but in the general case we have $\Delta_s(X) = \Delta_s(X, \sigma)$ and $\Delta_d = \Delta_d(\sigma)$. The light flux goes through the sensor and the different channels of the demodulator. For the cosine channel the analytical signal expression is

$$S(X) = \int_\sigma P(\sigma)\mathrm{d}\sigma + \frac{1}{2}U \times \int_\sigma P(\sigma)\cos 2\pi\sigma[\Delta_c(X, \sigma) - \Delta_d(\sigma)]\mathrm{d}\sigma, \tag{4.1}$$

which can be written as

$$S(X) = \tilde{P}(0) + \frac{1}{2}UI_3'.$$

Considering the $\sigma$ dependence of $\Delta_s$ and $\Delta_d$, we cannot identify $I_3'$ with $\tilde{P}(\Delta_s - \Delta_d)$. In the following sections we study how to compute $I_3'$ in some cases for various $\sigma$ dependences of $\Delta$.

##### A. Analytical Calculation

To compute $S(X)$, a complete knowledge of the functions $\Delta_s(X, \sigma)$, $\Delta_d(\sigma)$ is needed, and the existence of the integral $I_3'$ is assumed. However, it is possible, with certain assumptions on the linearization of $\Delta_s$ and $\Delta_d$ with respect to $\sigma$, to continue the development in specific cases.

Assumption 1: The continuous background is calibrated.

Assumption 2: In the useful spectral domain the visibility of the interferometers is constant and equal to one.

Assumption 3: The source power spectral density is symmetric around the central emission wave number. In the case of LED's assumption 2 is realistic.

Assumption 4: The spectral response of the photodetector is constant over the spectral bandwidth of the source. This assumption simplifies the analytical treatment and is a good approximation in the case of LED's. (The case of a nonsymmetric source has been studied, and for the typical emission spectra of LED's commonly used, the results are very close to those described in the following sections.)

Assumption 5: The phase between the cosine channel and sine channel is constant and equal to $\pi/2$ over the whole spectral range of the source.

With these five assumptions the recorded signals for the sine channel $S_s$ and the cosine channel $S_c$ are

$$S_s = \frac{1}{2}\left(S_0 - \frac{I_0}{I_1}S_1\right),$$

$$S_s = \mathrm{Im}\left\{\int_\sigma P(\sigma)\exp[2i\pi\sigma\Delta(X,\sigma)]\mathrm{d}\sigma\right\}, \quad (4.2a)$$

$$S_c = \frac{1}{2}\left(S_2 - \frac{I_0}{I_2}S_3\right),$$

$$S_c = \mathrm{Re}\left\{\int_\sigma P(\sigma)\exp[2i\pi\sigma\Delta(X,\sigma)]\mathrm{d}\sigma\right\}. \quad (4.2b)$$

We take

$$\phi(\sigma) = 2\pi\sigma[\Delta_s(X,\sigma) - \Delta_d(\sigma)]. \quad (4.3)$$

A Taylor expansion around $\sigma_0$ is

$$\phi(\sigma) = \phi(\sigma_0) + (\sigma - \sigma_0)\left(\frac{\partial\phi}{\partial\sigma}\right)_{\sigma_0} + \frac{1}{2}(\sigma - \sigma_0)^2\left(\frac{\partial^2\phi}{\partial\sigma^2}\right)_{\sigma_0} + \cdots. \quad (4.4)$$

Now we examine the influence of the different terms of $\phi(\sigma)$ on the computation of the $S_s$ and $S_c$ integrals.

### 1. *First Order*

In this case phase $\phi$ is simply linearized, so, taking

$$\Delta_0(X) = \Delta_s(X,\sigma_0) - \Delta_d(\sigma_0), \quad (4.5)$$

we obtain

$$\phi = 2\pi[\sigma_0\Delta_0 + (\sigma - \sigma_0)A] = \phi_0 + 2\pi A(\sigma - \sigma_0) \quad (4.6)$$

with

$$A(X) = \left[\frac{\partial}{\partial\sigma}\sigma\Delta(X,\sigma)\right]_{\sigma=\sigma_0} = \Delta_0(X) + \sigma_0\left[\frac{\partial\Delta(X,\sigma)}{\partial\sigma}\right]_{\sigma=\sigma_0}. \quad (4.7)$$

We easily obtain analytical signal expressions for signals $S_s$ and $S_c$:

$$S_s(X) = \tilde{P}(A)\sin(2\pi\sigma_0\Delta_0),$$

$$S_c(X) = \tilde{P}(A)\cos(2\pi\sigma_0\Delta_0). \quad (4.8)$$

Thus in this case we have $\phi_M = \phi_0$. When the phase dependence on $\sigma$ is linear, the measured phase is the same as if $\phi$ were independent of $\sigma$. However, Eqs. (4.8) show two effects on the modulation envelope of the sine and cosine channels.[11]

*First Effect:* The envelope peak is given for $A = 0$, i.e.,

$$\Delta_0(X) + \sigma_0\left[\frac{\partial\Delta(X,\sigma)}{\partial\sigma}\right]_{\sigma=\sigma_0} = 0,$$

and the point where the phase is equal to zero is obtained for $\Delta_0(X) = 0$. Therefore a shift appears between the signal envelope and the modulation. In the case of large shifts, to stay within the modulation envelope, the measurement must be effected at $|\Delta_0| \gg 0$, which induces a stronger sensitivity of the system to source central wavelength variations.

*Second Effect:* $A(X)$ is not equal to $\Delta_0(X)$. Therefore the modulation envelope given by $\tilde{P}(A)$ does not show the same half-height width as in the case of $\phi$ constant over the whole source emission spectrum. Assuming that the latter half-height width does not decrease too much, this effect is not really a problem.

### 2. *Second Order*

The expansion of Eq. (4.4) is performed to second order, i.e.,

$$\phi = \phi_0 + 2\pi A(\sigma - \sigma_0) + 2\pi B\frac{(\sigma - \sigma_0)^2}{2}, \quad (4.9)$$

with $A(X)$ given by Eq. (4.7) and

$$B(X) = \left[\frac{\partial^2}{\partial\sigma^2}\sigma\Delta(X,\sigma)\right]_{\sigma=\sigma_0}. \quad (4.10)$$

In this case we must compute the following integral:

$$I = \int_\sigma P(\sigma) \times \exp\left\{i\left[\phi_0 + 2\pi A(\sigma - \sigma_0) + 2\pi B\frac{(\sigma - \sigma_0)^2}{2}\right]\right\}\mathrm{d}\sigma. \quad (4.11)$$

The sources used in the device are LED's with known characteristics (central wave number, emission power $P_T$, and spectral bandwidth related to $\Delta\sigma$). The function $P(\sigma)$ is also known *a priori*. We take

$$P(\sigma) = \frac{P_T}{\Delta\sigma\sqrt{\pi}}\exp\{-[(\sigma - \sigma_0)/\Delta\sigma]^2\}. \quad (4.12)$$

After some developments we obtain

$$I = \frac{P_T\sqrt{\pi}}{\sqrt[1/4]{R}}\exp\left[-\left(\frac{\pi A}{\Delta\sigma\sqrt{R}}\right)^2\right] \times \exp\left[i\left(\phi_0 - \frac{\pi^3A^2B}{R} + \frac{1}{2}\arctan\theta\right)\right], \quad (4.13)$$

with

$$R = \frac{1}{(\Delta\sigma)^4} + (\pi B)^2,$$

$$\theta = \pi B(\Delta\sigma)^2.$$

We see that in this case the measured phase $\phi_M$ is not equal to $\phi_0$.

Equation (4.13) shows that when the phase has a quadratic dependence with $\sigma$, the measured phase $\phi_M$ is not equal to $\phi_0$ and the difference depends on the spectral width of the source, on the spectral dependence of the OPD's $\Delta_s$ and $\Delta_d$, and therefore on the parameter $X$ to be measured. The replacement of $\phi_M$ by $\phi_0$ leads to an error that reduces without data processing the system accuracy.

### 3. *nth Order*

When the expression of $\phi$ is performed to an order higher than 2, the analytical computation complexity of $S_s$ and $S_c$ dramatically increases. Moreover the spectral dependence of the birefringence of most crystals can be indefinitely expanded in $\sigma$ around a wave number $\sigma_0$, so that the presentation of each case is irrelevant. To predict the experimental results, we prefer a numerical simulation.

## B. Numerical Simulation

The numerical simulation consists of computing $S_s(X)$ and $S_c(X)$ with the help of a computer, which is possible if all the functions inside the integrals expressed by Eqs. (4.2) are analytically known. Then we obtain the measured phase $\phi_M$ for each value of $X$. In a first attempt we can use the preceding analytical approach to check and validate the results provided by the numerical simulation; then this simulation allows us to quantify in a rigorous way the effects from the spectral dependence of the birefringent materials used in the sensing and demodulation systems.

The analytical expression for $P(\sigma)$ is given in Eq. (4.12). For a Michelson-type sensor

$$\Delta_s(X, \sigma) = \Delta_s(X) = 2L, \tag{4.14}$$

where $L$ is the difference between the interferometer arms. For a birefringent-type sensor

$$\Delta_s(X, \sigma) = e\Delta n_s(T_s, X), \tag{4.15}$$

where $T_s$ is the sensor crystal temperature, $e$ is its thickness when used in the transmission mode, and $\Delta n_s$ is its birefringence. In the same way for a demodulator with polarimetric interference

$$\Delta_d(\sigma) = E\Delta n_d(T_d, \sigma), \tag{4.16}$$

where $T_d$ is the demodulator plate temperature, $E$ is the thickness, and $\Delta n_d$ is the birefringence. Functions $\Delta n_s$ and $\Delta n_d$ are either taken from tables (calcite from Ref. 12, potassium dihydrogen phosphate (KDP) from Ref. 13) or given by a formula [quartz from Ref. 14, lithium niobate ($LiNbO_3$) from Ref. 13].

Because of the infinitesimal effects that we want to display and the importance of high resolution on the phase to be measured, the numerical computation requires high precision. For $S_s$ and $S_c$ an oscillating function is integrated on the bound interval where the spectral power density function is not negligible. An efficient method for this computation is the 30-point G–61-point Kronrod method that gives in this case $10^{-12}$ relative precision.

## C. Validation of the Numerical Simulation

To test the numerical computation, we can compare the difference $\phi_M - \phi_0$ obtained with the simulation and the difference $\phi_M - \phi_0$ given by the analytical computation for the same setup configuration and the same parameter $X$ scale. Here we consider two configurations:

(1) A Michelson-type sensor coupled with a polarimetric demodulator. Here the parameter to be measured is the interferometer arm-length difference $L$. So in this case

$$\phi = 2\pi\sigma[2L - E\Delta n_d(T_d, \sigma)] = 2\pi\sigma\Delta(L, \sigma). \tag{4.17}$$

(2) A birefringent sensor coupled with the same demodulator. In this case the parameter to be measured is the crystal temperature used in the sensor $T_s$. So in this case

$$\phi = 2\pi\sigma[e\Delta n_s(T_s, \sigma) - E\Delta n_d(T_d, \sigma)] = 2\pi\sigma\Delta(T_s, \sigma). \tag{4.18}$$

We first study the case in which $\phi$ is linearized in $\sigma$. Theoretically the expressions for the recorded signals are given by Eqs. (4.8). The $X$ scale is chosen to have $m(\phi) \gg 0$. Thus in this range

$$\tilde{P}(A) \neq 0. \tag{4.19}$$

Denoting $X_m$ and $X_S$ as the extremal values means that $|A(X_m)| \ll l_c$ and $|A(X_S)| \ll l_c$, where $l_c$ represents the source coherence length. For both cases the analytical development gives $\phi_M = \phi_0$ for $X_m \leq X_i \leq X_S$. The first computed results were obtained for each value $X_i$ of $X$ in the scale domain. Figure 2 shows the difference $\phi_0(X_i) - \phi_M(X_i)$ from the approximate phase $\phi_0(X_i)$ for the two sensor types with $\sigma_0 = 1.189\ \mu m^{-1}$, $\Delta\sigma = 72 \times 10^{-3}\ \mu m^{-1}$, and $E = e = 25$ mm. $T_s \in (0, 100°C)$ for the birefringent sensor, and $L \in (115, 121\ \mu m)$ for the Michelson-type sensor. In both cases $T_d = 20$ °C. To simulate a possible real case the birefringence functions $\Delta n_s(T, \sigma)$, $\Delta n_d(T, \sigma)$ are chosen for the best quartz characteristic approxi-

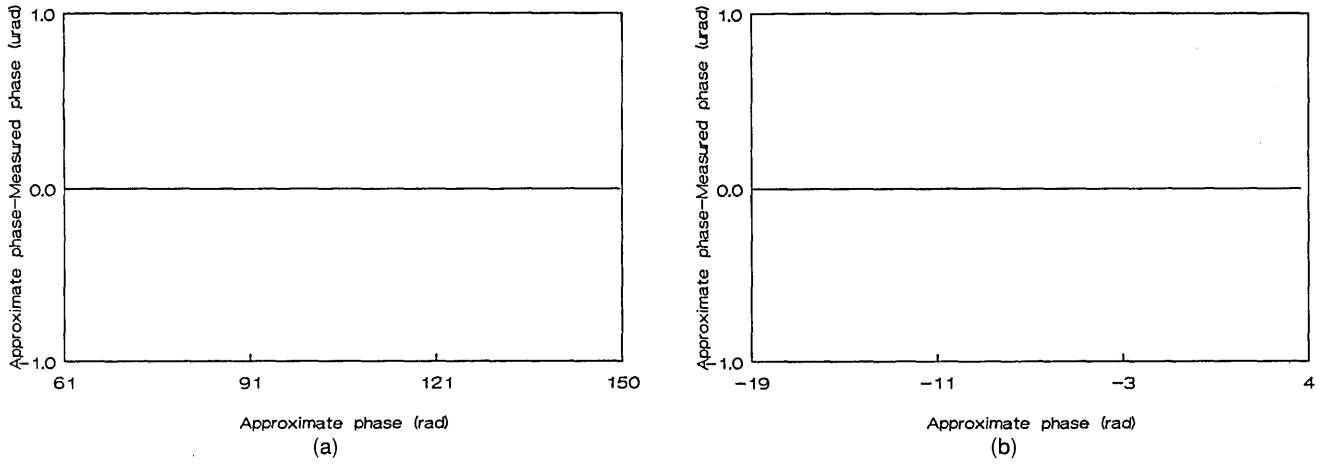


Fig. 2. Influence of the chromatic dispersion of the OPD on the measured phase. Comparison between the analytical approach and the numerical computation for first-order expansion: (a) Michelson-type sensor, (b) birefringent sensor.

mation (birefringence $\Delta n_q$). So

$$\Delta n_s(T, \sigma_0) = \Delta n_q(T, \sigma_0),$$
$$\Delta n_d(T, \sigma_0) = \Delta n_q(T, \sigma_0), \tag{4.20}$$

$$\left[\frac{\partial}{\partial\sigma}\Delta n_s(T, \sigma)\right]_{\sigma=\sigma_0} = \left[\frac{\partial}{\partial\sigma^2}\Delta n_q(T, \sigma)\right]_{\sigma=\sigma_0},$$

$$\left[\frac{\partial}{\partial\sigma}\Delta n_d(T, \sigma)\right]_{\sigma=\sigma_0} = \left[\frac{\partial}{\partial\sigma}\Delta n_q(T, \sigma)\right]_{\sigma=\sigma_0}. \tag{4.21}$$

For both cases there is perfect agreement between the analytical calculation and the numerical simulation. The difference $\phi_M - \phi_0$ is quasi-null on the parameter range (as high as the computational precision).

Now we study the second-order expansion case. In this case $\phi$ is given by Eq. (4.9). Figure 3 shows the same kind of result as in Fig. 2 but for a second-order expansion. The demodulation crystal characteristics are those given by Eqs. (4.20) and (4.21) with, in addition,

$$\left[\frac{\partial^2}{\partial\sigma^2}\Delta n_s(T, \sigma)\right]_{\sigma=\sigma_0} = \left[\frac{\partial^2}{\partial\sigma^2}\Delta n_q(T, \sigma)\right]_{\sigma=\sigma_0},$$

$$\left(\frac{\partial^2}{\partial\sigma^2}\Delta n_d(T, \sigma)\right)_{\sigma=\sigma_0} = \left[\frac{\partial^2}{\partial\sigma^2}\Delta n_q(T, \sigma)\right]_{\sigma=\sigma_0}. \tag{4.22}$$

Here again good agreement is found between the analytical result and the numerical simulation. Moreover we can see that in both cases the results with the second-order expansion are close to those obtained for the complete expansion ($n$th order), which means that in the two preceding configurations the second-order expansion is sufficient to describe the effects of chromatic dispersion on the phase linearity.

Note that in Fig. 3(b) the particular point $M_0(\phi_0, 0)$ belongs to all lines. At this point both temperatures in the sensor and the demodulator are equal:

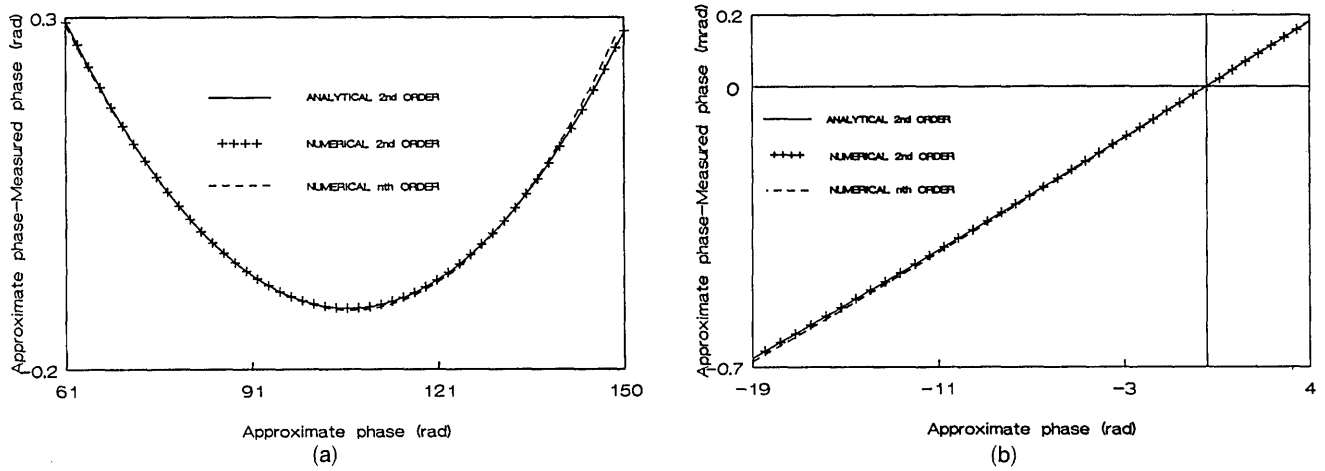


Fig. 3. Influence of the chromatic dispersion of the OPD on the measured phase. Comparison among the analytical approach, the numerical computation for second-order expansion, and the numerical computation for $n$th-order expansion: (a) Michelson-type sensor, (b) birefringent sensor.

$A(T_s = T_d) = B(T_s = T_d) = 0$ and $\phi(T_s = T_d, \sigma) = \phi_0 = 0$ and at $M_0$, $\phi_M = \phi_0$.

In light of these results for all configurations the difference $\phi_M - \phi_0$ appears to be clearly a result of the nonlinear $\sigma$ dependence of phase $\phi$.

### D. Real Operating Prevision

Assuming that analytical expressions for the functions in Eqs. (4.2) are sufficiently good approximations, one can use a numerical simulation to choose the system dimension. For example, one evaluates the spectral dependence influence of the system crystal birefringence on the measured phase linearity. Figure 4 shows the computed differential phase $\Delta\phi$ function of the sensor OPD for a Michelson-type sensor and a quartz demodulator plate ($E = 25$ mm) and with the two sources such as $\sigma_1 = 1.189\ \mu m^{-1}$, $\Delta\sigma_1 = 72.10^{-3}\ \mu m^{-1}$, $\sigma_2 = 1.17\ \mu m^{-1}$, $\Delta\sigma_2 = 64 \times 10^{-3}\ \mu m^{-1}$. There is a strong nonlinearity for each source. Because of this phenomenon the use of $\Delta\phi$ to obtain the interferometer order can lead to errors in $p_1$ and errors in the measurement. To avoid this problem, it is necessary either to perform a numerical correction on the measured phase or to choose a well-adapted spectral configuration.

#### 1. *Research of the Optimal Configuration*

We know that the difference between $\phi_M$ and $\phi_0$ is due to the second- or superior-order term in the expansion of $\phi$ in $\sigma$ around $\sigma_0$. To reduce this problem, a solution consists in using in the demodulator a crystal whose birefringence shows the same chromatic dispersion as the one of the sensor. We saw in Subsection 4.A.2 that the difference $\phi_0 - \phi_M$ depends strongly on the quadratic term in the expansion of $\phi$. The parameter $B'$ with

$$B' = \frac{1}{\Delta n}\left[\frac{\partial^2}{\partial\sigma^2}\Delta n(T, \sigma)\right]_{\sigma_0}\Bigg|, \tag{4.23}$$

characterizes the second-order spectral performance of a crystal whose birefringence is $\Delta n$ and whose temperature is $T$. Table 1 shows the values of $B'$ for quartz, $LiNbO_3$, calcite, and KDP. The best crystal for spectral performances for our study is that whose value of $B'$ is the smallest. In this case the best choice is calcite.

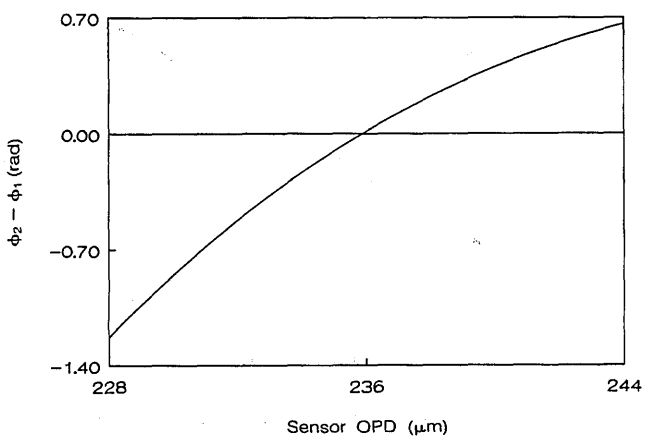


Fig. 4. Influence of the chromatic dispersion of the OPD on the differential phase linearity. Quartz demodulator plate.

Table 1. Spectral Characteristics of Some Birefringent Crystals

| Crystals | $B'(\mu m^2)(\sigma_0 = 1.189\ \mu m^{-1})$ |
|---|---|
| Quartz | $9.02 \times 10^{-2}$ |
| $LiNbO_3$ | $2.18 \times 10^{-1}$ |
| Calcite | $6.83 \times 10^{-2}$ |
| KDP | $4.05 \times 10^{-1}$ |

For a birefringent sensor, to reduce the spectral dependence of $\phi$, it is convenient to use in the demodulator the same crystal as in the sensor. So Eq. (4.18) becomes

$$\phi = 2\pi\sigma e[\Delta n_s(T_s, \sigma) - \Delta n_d(T_d, \sigma)].$$

However, a residual spectral dependence persists because of the temperature difference $T_s - T_d$ between the sensor and the demodulator. It is convenient to fix the demodulator temperature $T_d$ equal to the average value of the sensor temperature range.

For a Michelson-type sensor Eq. (4.17) gives the phase expression. For the usual birefringent crystals this condition cannot be realized. However, a good approximation is obtained when one uses different birefringent crystal associations and adjusts their respective thicknesses correctly. According to Subsection 4.A, to reduce $\phi_M - \phi_0$ we need

$$\left(\frac{\partial^2\phi}{\partial\sigma^2}\right)_{\sigma=\sigma_0} = 0. \tag{4.24}$$

In this case Eq. (4.24) is equivalent to

$$\left(\frac{\partial^2\sigma\Delta n_d}{\partial\sigma^2}\right)_{\sigma=\sigma_0} = 0. \tag{4.25}$$

Here we consider only the association of two birefringent crystals. We denote $e_1$, $e_2$ as their thicknesses and $\Delta n_1$, $\Delta n_2$ as their birefringences. When we take

$$K = \frac{\left(\frac{\partial^2\sigma\Delta n_1}{\partial\sigma^2}\right)_{\sigma_0}}{\left(\frac{\partial^2\sigma\Delta n_2}{\partial\sigma^2}\right)_{\sigma_0}}, \tag{4.26}$$

Eq. (4.24) becomes

$$e_1 + \varepsilon K e_2 = 0, \tag{4.27}$$

with $\varepsilon = +1$ or $\varepsilon = -1$ if the optical axes of the crystals are aligned or crossed, respectively. The composite crystal plate birefringence $\Delta n_d$ is then

$$\Delta n_d = \frac{\Delta n_1 - K\Delta n_2}{1 - \varepsilon K}. \tag{4.28}$$

For technological reasons we prefer $K \approx 1$ ($e_1 \approx e_2$). These considerations lead to a composite calcite/KDP crystal plate with $K = -3.622$ ($\varepsilon = +1$ is for the aligned optical axes). Figure 5 is obtained with the numerical simulation; it shows the difference between $\phi_M$ and $\phi_0$ as a function of $\phi_0$ for a Michelson-type sensor both for a composite calcite/KDP demodulator plate ($K = -3.622$, $E = 3.013$ mm) and for a quartz demodulator plate ($E = 25$ mm) with a source such that $\sigma_0 = 1.189\ \mu m^{-1}$ and $\Delta\sigma = 72 \times 10^{-3}\ \mu m^{-1}$. The right-hand scale corresponds to the dashed curve. Note that the use of a composite plate permits a significant reduction in the difference between $\phi_M$ and $\phi_0$. Figure 6 shows the same results as in Fig. 4 for a composite calcite/KDP demodulator plate. The linearity of the differential phase increases as expected.

However, in a practical technological realization, to avoid the use of temperature stabilization, the demodulator must introduce a stable OPD with respect to $T_d$. Then

$$\left(\frac{\partial \sigma \Delta n_d}{\partial T}\right)_{\sigma_0, T_d} \approx 0. \tag{4.29}$$

This condition leads to the use of a composite calcite/KDP birefringent plate with $K = 0.982$ ($\varepsilon = -1$).[15] For such a plate we describe in Fig. 7 $\phi_M - \phi_0$ as a function of $\phi_0$; we note that in this case this difference is comparable with that of a quartz demodulator plate. The choice of the crystal demodulator plate results from a compromise between the spectral performance and sensitivity of $\Delta_d$ to the temperature.

### 5. Influence of the Chromatic Dispersion of the $\pi/2$ Retarder

In the demodulator presented the sine channel is obtained by addition of a $\pi/2$ retarder with respect to the cosine channel. So far we have supposed that the retardation was equal to $\pi/2$ over the whole source emitted spectrum. However, the use of broadband sources makes this condition difficult to realize, which has disturbing effects on the differential phase.

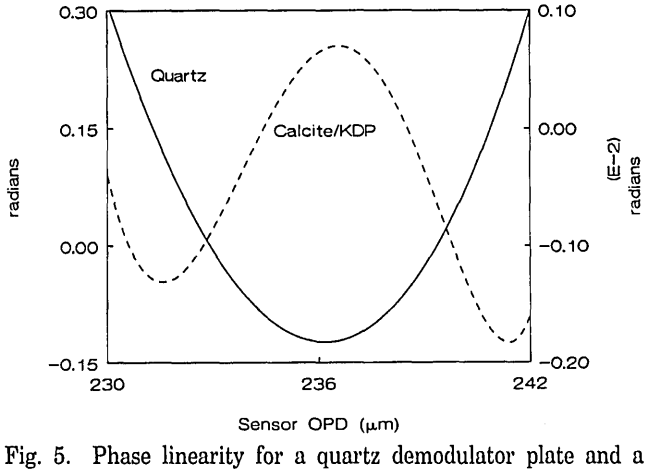


Fig. 5. Phase linearity for a quartz demodulator plate and a composite calcite/KDP ($K = -3622$) demodulator plate.

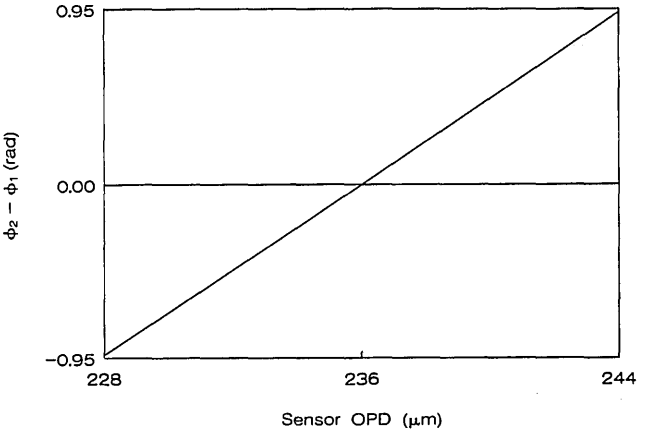


Fig. 6. Influence of the OPD chromatic dispersion on the differential phase linearity. Calcite/KDP ($K = -3622$).

#### A. Analytical Calculation

We will develop an analytical approach with assumptions 1–4 of Subsection 4.A plus assumption 5; the two OPD's $\Delta_s$ and $\Delta_d$ are not $\sigma$ dependent.

After calibration the formed cosine signal expression is

$$S_c(X) = \tilde{P}(\Delta_s - \Delta_d)\cos[2\pi\sigma_0(\Delta_s - \Delta_d)]. \tag{5.1}$$

We denote $\Delta_L(\sigma)$ as the OPD introduced by the retarder of the sine channel. Thus the corresponding phase $\phi_L$ is

$$\phi_L(\sigma) = 2\pi\sigma\Delta_L(\sigma), \tag{5.2}$$

and the sine signal expression is

$$S_s(X) = \int_\sigma P(\sigma)\cos 2\pi\sigma[\Delta_s(X) - \Delta_d - \Delta_L(\sigma)]d\sigma. \tag{5.3}$$

##### 1. *Constant Retardation*

If, for example, $\phi_L(\sigma)$ is such that $\phi_L(\sigma) = \pi/2$, which corresponds to the ideal case of an achromatic retarder, we have

$$S_s(X) = \tilde{P}(\Delta_s - \Delta_d)\sin 2\pi\sigma_0(\Delta_s - \Delta_d)$$

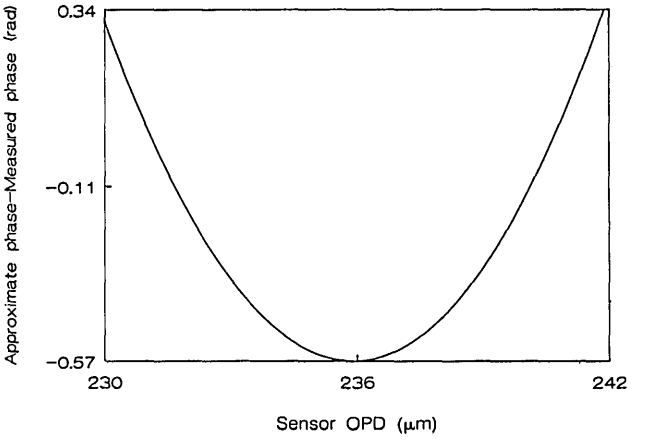


Fig. 7. Phase linearity for an athermal demodulator plate.

and $\phi_M = \phi_0$. In this case the measured phase is equal to the approximate one.

### 2. *Linear σ-Dependent Retardation*

If $\phi_L$ is not constant over the entire emitted spectrum, the integral expressed by Eq. (5.3) has no simple analytical solution. We write the equation as

$$\phi_L(\sigma) = \frac{\pi}{2} + 2\pi A(\sigma - \sigma_0), \tag{5.4}$$

where $A$ is as given in Eq. (4.7). Noting that

$$A_L' = \sigma_0\left[\frac{\partial \Delta_L(\sigma)}{\partial \sigma}\right]_{\sigma_0}, \tag{5.5}$$

we obtain

$$S_s(X) = \tilde{P}(\Delta_s - \Delta_d - A_L')\sin[2\pi\sigma_0(\Delta_s - \Delta_d)], \tag{5.6}$$

$$\phi_M = \tan^{-1}\left[\frac{\tilde{P}(\Delta_s - \Delta_d - A_L')}{\tilde{P}(\Delta_s - \Delta_d)}\tan\phi_0\right]. \tag{5.7}$$

Then $\phi_M \neq \phi_0$. There is a shift between the sine modulation envelope and the cosine one. The replacement of $\phi_M$ by $\phi_0$ leads to a systematic error, depending on the parameter to be measured. This phenomenon has a dramatic effect on the order $p_1$ determination. Therefore we will study differential phase $\Delta\phi$.

We denote $\sigma_1$ and $\sigma_2$, the two central source wave numbers; $\Delta\sigma_1$ and $\Delta\sigma_2$ their half-height widths; and $P_{T1}$ and $P_{T2}$, their total emitted powers. Thus

$$P_1(\sigma) = \frac{P_{T1}}{\Delta\sigma_1\sqrt{\pi}}\exp\{-[(\sigma - \sigma_1)/\Delta\sigma_1]^2\},$$

$$P_2(\sigma) = \frac{P_{T1}}{\Delta\sigma_2\sqrt{\pi}}\exp\{-[(\sigma - \sigma_2)/\Delta\sigma_2]^2\}. \tag{5.8}$$

Noting that

$$\phi_1 = 2\pi\sigma_1\Delta,$$

$$\phi_2 = 2\pi\sigma_2\Delta, \tag{5.9}$$

we write the expression for the measured differential phase $\Delta\phi_M$ as

$$\Delta\Phi_M = \tan^{-1}\left(\frac{\exp\{-[\pi\Delta\sigma_2(\Delta - A_L')]^2\}}{\exp[-(\pi\Delta\sigma_2\Delta)^2]}\tan\phi_2\right) - \tan^{-1}\left(\frac{\exp\{-[\pi\Delta\sigma_1(\Delta - A_L')]^2\}}{\exp[-(\pi\Delta\sigma_1\Delta)^2]}\tan\phi_1\right) \tag{5.10}$$

and $\Delta\phi_M \neq \phi_2 - \phi_1$. So, in the case of a linear $\sigma$ dependence of $\phi$, it is possible to compute $\Delta\phi_M$ analytically. For a more complete expansion of $\phi$ in $\sigma$, a numerical simulation is required.

### B. Validation of the Numerical Simulation

As in Subsection 4.B, to validate the numerical results we compare them to analytical results in some simple cases. Here $\Delta_s = \Delta_s(X)$ and $\Delta_d = \Delta_d(T_d)$. Figure 8 shows a comparison between the analytical and the numerical results for $\Delta_L(\sigma) = 1/4\sigma_0$ with $\sigma_0 \approx (\sigma_1 + \sigma_2)/2$; in this case

$$\phi_L(\sigma) = \frac{\pi}{2} + (\sigma - \sigma_0)\frac{1}{4\sigma_0}. \tag{5.11}$$

For two sources such as $\sigma_1 = 1.189\ \mu m^{-1}$, $\Delta\sigma_1 = 72 \times 10^{-3}\ \mu m^{-1}$; $\sigma_2 = 1.17\ \mu m^{-1}$, $\Delta\sigma_2 = 64 \times 10^{-3}\ \mu m^{-1}$, and a Michelson-type sensor with a quartz demodulator plate ($E = 25$ mm), we see perfect agreement between analytical and numerical results. Without more complicated data processing the nonmonotony of the differential phase can produce fatal errors for the $p_1$-order determination. For a real operating system and for an acceptable differential phase-error determination, a numerical simulation can also be used to choose characteristic parameters of the system (the range, coherence length of the sources, birefringent materials, retarders, etc.). However, to eliminate this drawback, it is possible to take some achromatic or quasi-achromatic retarders currently used in optics:

The Fresnel rhomb is strongly achromatic, but for a $\pi/2$ retarder configuration the optic ray is shifted. Moreover a setup of this kind of retarder requires high precision.

Composite retardation plates are made up of two or more birefringent elements. These retarders are partially achromatic but their setup is easy.[16]

Figure 9 shows computed differential phases for three retarders. The nonlinearity of $\Delta\phi$ increases with the chromatic dispersion of the retarder.

## 6. Experimental Evidence of the Theoretical Effects

The experimental setup is shown in Fig. 10. The fluxes emitted by the two sources ($\sigma_1 = 1.189\ \mu m^{-1}$,

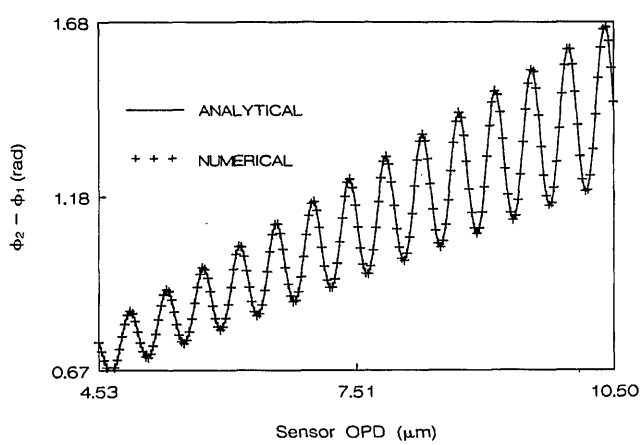


Fig. 8. Influence of the chromatic dispersion of the retarder on the differential phase linearity. Comparison between the analytical approach and numerical computation.

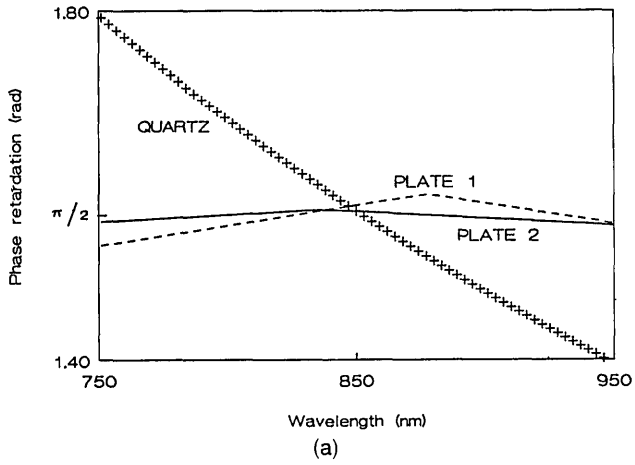


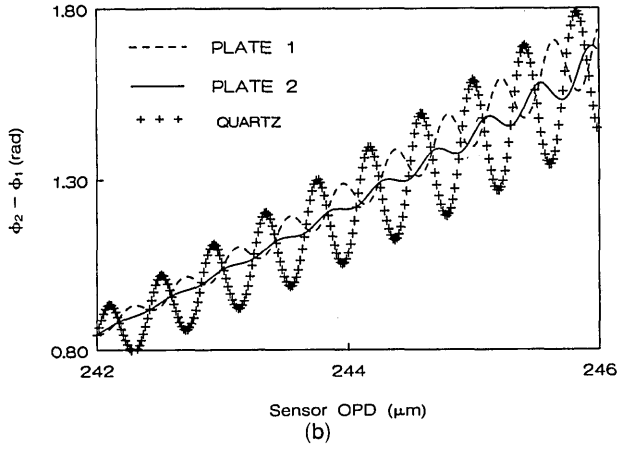


Fig. 9. Influence of the chromatic dispersion of some retarders: (a) phase retardations, (b) corresponding differential phases when the retarders are used in the sine channel.

$\Delta\sigma_1 = 72 \times 10^{-3}\ \mu m^{-1}$; $\sigma_2 = 1.17\ \mu m^{-1}$, $\Delta\sigma_2 = 64 \times 10^{-3}\ \mu m^{-1}$) are sent by multimode optical fiber and then go through the sensor and the demodulator. The demodulator optical outputs are sent to photodetectors through four optical fibers to make the setting of the various elements during the experiment easier. (This configuration is not recommended because it makes the system sensitive to line-loss variations.) The eight available signals (four channels, two sources) are 16 bit digitized, recorded on a computer, and processed with the data calculated during the calibration. Thus we can compute information related to the sensor (the phase, the differential phase, the parameter to measure). The computer also drives through a digital-to-analog (D/A) conversion card, a piezoelectric displacement integral with one of the Michelson arms. Thus the sensor OPD can be changed easily. In Subsections 6.A–6.C the $\pi/2$ retarder is a Fresnel rhomb.

Preliminary Note: In the present case the use of a chromatic demodulator crystal plate induces a difference between $\phi_1$ and $\phi_2$. With the linear approximation we have

$$\phi_1 = \phi_0 + 2\pi A(\sigma_1 - \sigma_0),$$
$$\phi_2 = \phi_0 + 2\pi A(\sigma_2 - \sigma_0), \qquad (6.1)$$

where $A$ is as in Eq. (4.7). Then

$$\Delta\phi = 2\pi(\sigma_1 - \sigma_2)\Delta(\sigma_0) + \Omega, \qquad (6.2)$$

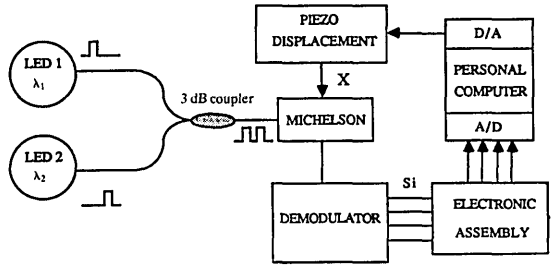


Fig. 10. Experimental setup.

with

$$\Omega = 2\pi(\sigma_1 - \sigma_2)A. \qquad (6.3)$$

Introducing the term $\Omega$ in the order $p_1$ calculation, we can compute $\phi_1$ and then $\Delta_s$ with

$$\Delta_s = \frac{\phi_1}{2\pi\sigma_1} + \Delta_d(\sigma_1). \qquad (6.4)$$

### A. Shift Effect

From the analytical results the shift between the correlation signal envelope and the point where $\phi_1$ is equal to zero is obtained with Eq. (4.13). For a quartz demodulator plate with thickness $E = 25$ mm the shift corresponds to a Michelson OPD $d_t \approx 12.4$ μm. Figure 11 shows the recorded correlation peak for a voltage ramp on the piezoelectric stack and the corresponding measured OPD. The shift experimentally obtained is $d_e \approx 12.6$ μm (1 V corresponds approximately to an OPD variation of 8.4 nm).

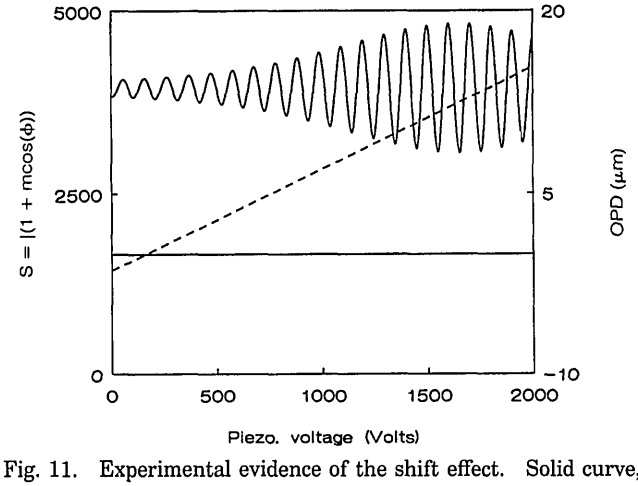


Fig. 11. Experimental evidence of the shift effect. Solid curve, correlation peak; dashed curve, corresponding measured phase.

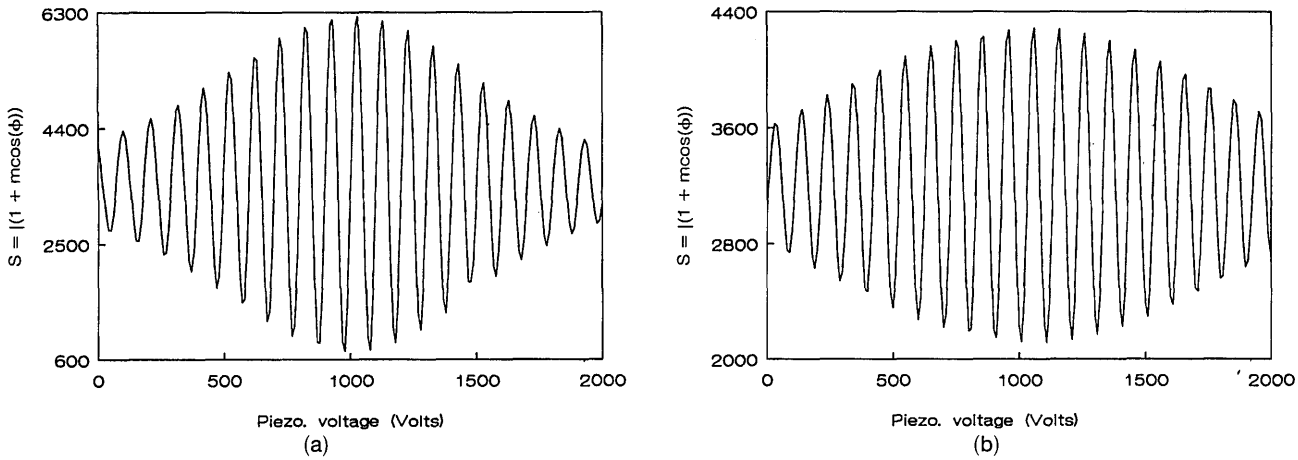


Fig. 12. Experimental evidence of the broadening effect: (a) recorded central peak, (b) recorded correlation peak.

### B. Broadening Effect

According to Section 2, signal $S$ at the output of a photodetector placed at the output of a Michelson interferometer with $\Delta_c \ll l_c$ is given by

$$S = \widetilde{P(0)} + u_s \widetilde{P(\Delta_s)}. \tag{6.5}$$

For a Gaussian source shape described by Eq. (4.12) the width for a 3/4 amplitude of the signal envelope, which is not affected by the broadening effect described in Subsection 4.A is obtained for a Michelson OPD variation $2\Delta L_{3/4}$ such as

$$2\Delta L_{3/4} = 2\,\frac{[-\ln(3/4)]^{1/2}}{\pi\Delta\sigma}\cdot \tag{6.6}$$

For a second-order approximation (Subsection 4.A.2), when the Michelson interferometer is coupled to a birefringent demodulation interferometer, the signal given by a photodetector is obtained by Eq. (4.13) and has a location-dependent width[17]:

$$2\Delta L_{3/4} = 2\Delta\sigma\,\frac{[-\ln(3/4)]^{1/2}}{\pi}\sqrt{R}. \tag{6.7}$$

Figure 12 was obtained for a Michelson interferometer coupled to a birefringent quartz interferometer with $E = 25$ mm and $T_d = 20$ °C. The envelope is clearly broadened in Fig. 12(b), which shows the secondary peak, compared with Fig. 12(a), which shows the central peak. In this case we measure $2\Delta L_{3/4} \approx 9$ μm when Eq. (6.7) gives $2\Delta L_{3/4} = 9.15$ μm.

### C. Difference between the Approximate Phase and Measured Phase

We know that the birefringence spectral dependence introduces a difference between the measured phase and the approximate phase. Figure 13 shows the comparison between $\phi_M - \phi_0$ experimentally measured and numerically simulated for two demodulator plates in quartz ($E = 25$ mm) and in $LiNbO_3$ ($E = 3.16$ mm).

### D. Nonlinearity of the Differential Phase

Figure 14 shows a comparison between the computed differential phase and the measured one for a quarter-wavelength plate in quartz and a demodulator plate in quartz ($E = 24$ mm).

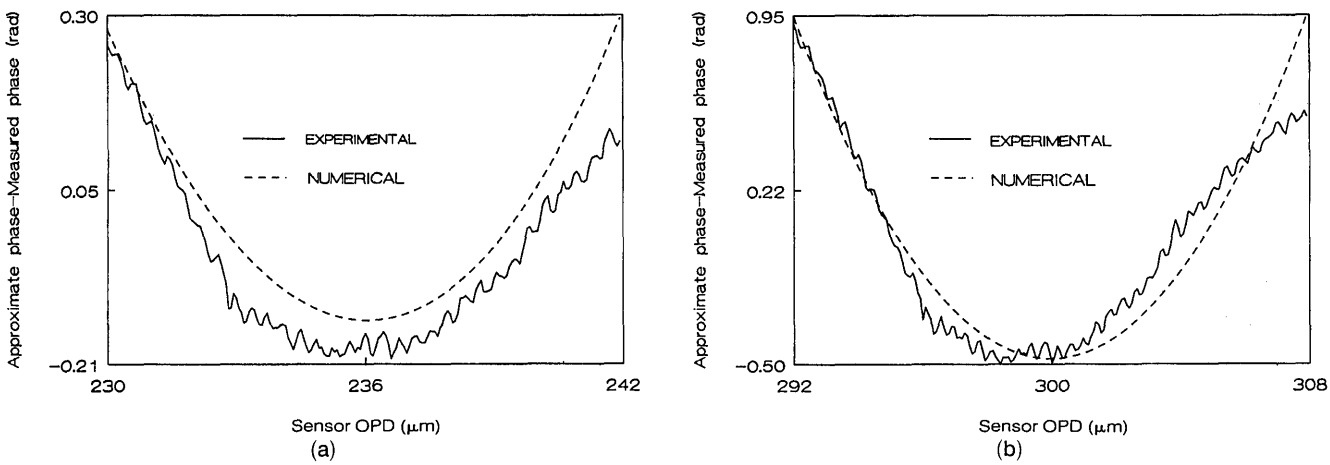


Fig. 13. Experimental evidence of the influence of the chromatic dispersion of the OPD on the measured phase: (a) demodulator plate in quartz, (b) demodulator plate in $LiNbO_3$.

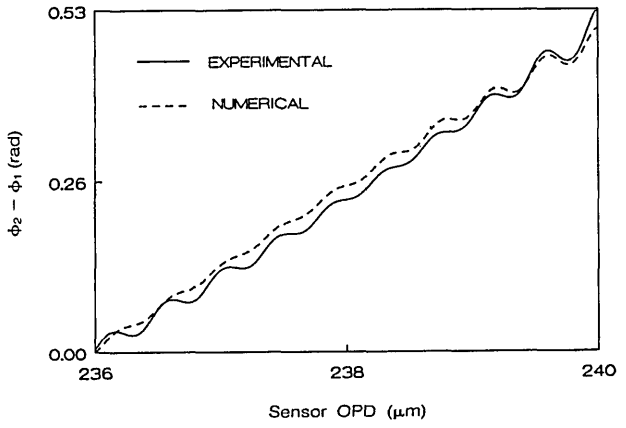


Fig. 14. Experimental evidence of the influence of the chromatic dispersion of the retarder on the differential phase linearity.

## 7. Practical Realizations

All the preceding considerations have led to the development of the ACCORD system,[18] which has been used to demodulate temperature and pressure sensors for down-hole applications[19] and for OSTIC/OSMOS strain sensors described by Sansonetti *et al.*[20] Figure 15 shows an experimental temperature sensor calibration with chromatic OPD effects totally neglected; it also shows that the temperature measurement improves when the demodulator plate and the sine channel retarder are strongly achromatic.

Note: For industrial applications it is necessary to consider the fact that the spectral envelope of LED's varies as a function of device temperature and device age. Because of the calibration of the dc components described in Secion 3, the change in this parameter does not influence the phase measurement. The half-height-width variations lead to second-order effects on the phase measurement and influence only the linearity of the phase. The central wavelength fluctuations dramatically influence the measurement, so for industrial applications the LED's are cooled. The use of an interferometric filter to select a stable spectrum is another solution to the problem of $\lambda_0$ variations, because for this kind of device $(\partial\lambda_0)/\partial T = 0.03$ nm/°C is 1 order of magnitude less than for LED's.

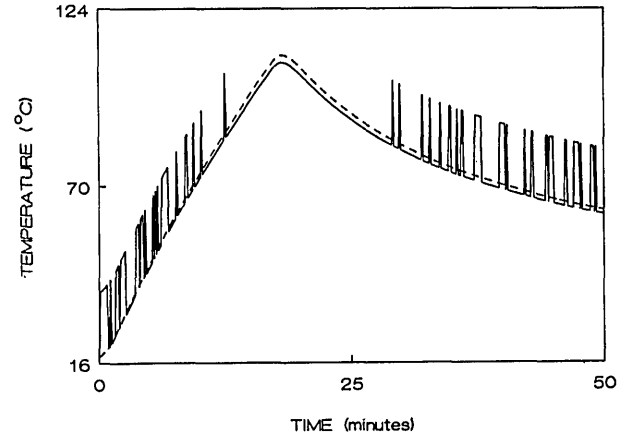


Fig. 15. Influence of the correction of the chromatic OPD effects on the measurement. Solid curve, quartz demodulator plate and mica retarder in the sine channel; dashed curve, demodulator plate and sine channel retarder strongly achromatic.

## 8. Conclusion

The effects of the chromatic dispersion of both OPD and $\pi/2$ retardation in a dual interferometer measurement device have been analyzed. Good agreement among analytical calculation, numerical simulation, and experimental results has been found, which enables us to choose the best configuration of the system for a given performance in terms of phase resolution. Using the analytical results, one finds that it is also possible to utilize more precise data processing than that described in Section 2 to recover the correct value of the parameter to be measured. These considerations have led to the development of the ACCORD system. This detection unit gives a rms phase-noise performance of better than 150 μrad $(\text{Hz})^{-1/2}$ and an accuracy of 1 mrad over a $40\pi$ phase range.[17] Moreover it has been shown that actually the rms noise is mainly a result of the binary modulation of the sources. With a sine amplitude modulation it has been shown that the rms noise performance should be better than 10 μrad $(\text{Hz})^{-1/2}$. This performance can be compared with that of heterodyne interferometers but with a broadband light source.

## References

1. J. P. Goedgebuer, H. Porte, and A. Hamel, "Electro-optic modulation of multilongitudinal mode laser diodes: demonstration at 850 nm with simultaneous data transmission by coherence multiplexing," IEEE J. Quantum Electron. **QE-23,** 1135–1144 (1987).
2. R. Ulrich, "Theory of spectral encoding for fiber optic sensors," in *Proceedings of the NATO Advanced Study Institute on Optical Fiber Sensors,* M. Nijhoff, ed. (NATO Advanced Study Institute, Erice, Italy, 1986), pp. 73–130.
3. P. Dabkiewicz and R. Ulrich, "Spectral encoding for fiber-optic industrial sensors," in *Proceedings of the Third European Fiber Optic Communications and Local Area Networks Exposition* (Information Gatekeepers, Boston, Mass., 1985), pp. 212–217.
4. Th. Bosselman and R. Ulrich, "High-accuracy position sensing with fiber-coupled white-light interferometers," in *Proceedings of the Second International Conference on Optical Fiber Sensors,* M. Nijhoff, ed. (Springer-Verlag, Stuttgart, Germany, 1984), pp. 361–364.
5. F. Farahi, T. P. Newson, J. D. C. Jones, and D. A. Jackson, "Coherence multiplexing of remote fiber optic Fabry–Perot sensing system," Opt. Commun. **65,** 319–331 (1988).
6. J. T. Freidah, R. F. Cahill, A. A. Joseph, H. B. Turner, S. A. Holmes, and R. E. Wagoner, "Passive homodyne optical grating demodulator: principles and performance," in *Proceedings of the Third International Conference on Fiber Optic and Laser Sensors III,* E. L. Moore and O. G. Ramer, eds., Proc. Soc. Photo-Opt. Instrum. Eng. **566,** 114–121 (1985).
7. C. Polhemus "Two-wavelength interferometry," Appl. Opt. **12,** 2071–2074 (1973).
8. D. A. Jackson, A. D. Kersey, and A. C. Lewin, "Fiber gyroscope with passive quadrature detection," Electron. Lett. **20,** 399–401 (1984).

9. Y. Y. Cheng and J. C. Wyant, "Two-wavelength phase shifting interferometry," Appl. Opt. **23,** 4539–4543 (1984).
10. K. Creath, "Step height measurement using two wavelength phase-shifting interferometry," Appl. Opt. **26,** 2810–2816 (1987).
11. C. Mariller and M. Lequime, "Fiber-optic 'white-light' birefringent temperature sensors," in *Proceedings of the Second International Conference on Fiber Optic Sensors II,* A. M. Scheggi, ed., Proc. Soc. Photo-Opt. Instrum. Eng. **798,** 121–130 (1987).
12. W. G. Driscoll and W. Vaughan, eds., *Handbook of Optics* (McGraw-Hill, New York, 1978), Chap. 10, p. 10.26.
13. F. Zernike and J. E. Midwinter, *Applied Nonlinear Optics* (Wiley, New York, 1973), Chap. 4, p. 90.
14. J. Macé de Lépinay, "Détermination des constantes optiques pour la radiation verte du mercure—leur application aux mesures d'épaisseur par la méthode de Mouton," J. Phys. Theor. Appl. **9,** 644–652 (1900).
15. M. Lequime, C. Mariller, and H. Giovanni, "Appareil optoélectronique de mesure à distance d'une grandeur physique," French patent 8,907,856 (14 June 1989).
16. Ref. 12, pp. 10.115–10.119.
17. E. Brinkmeyer and R. Ulrich, "High-resolution OCDR in dispersive waveguides," Electron. Lett. **20,** 413–414 (1990).
18. M. Lequime, C. Lecot, H. R. Giovannini, and S. J. Huard, "A dual-wavelength passive-homodyne detection unit for fiber-coupled white-light interferometers," in *Proceedings of the Fourth International Conference on Fiber Optic Sensors IV,* R. T. Kersten, ed., Proc. Soc. Photo-Opt. Instrum. Eng. **1267,** 288–298 (1990).
19. M. Lequime, C. Lecot, P. Jouve, and J. Pouleau, "Fiber optic pressure and temperature sensor for down-hole applications," in *Proceedings of the Fifth International Conference on Fiber Optic Sensors: Engineering and Applications,* A. J. Bruinsma and B. Culshaw, eds., Proc. Soc. Photo-Opt. Instrum. Eng. **1511,** 244–247 (1991).
20. P. Sansonetti, J. J. Guerin, M. Lequime, and J. Debrie, "Parallel coherence receiver for quasi-distributed optical sensor," in *Proceedings of the Fourth International Conference on Fiber Optic Smart Structures and Skins IV,* R. O. Claus and E. Udd, eds., Proc. Soc. Photo-Opt. Instrum. Eng. **1588,** 143–149 (1991).